

Sparse imaging for fast electron microscopy

Hyrum S. Anderson^{*1}, Jovana Ilic-Helms², Brandon Rohrer¹, Jason Wheeler¹, Kurt Larson¹

Sandia National Laboratories[†]

¹P.O. Box 5800, Albuquerque, NM 87185

²P.O. Box 969, Livermore, CA 94551-0969

Abstract. Scanning electron microscopes (SEMs) are used in neuroscience and materials science to image centimeters of sample area at nanometer scales. Since imaging rates are in large part SNR-limited, large collections can lead to weeks of around-the-clock imaging time. To increase data collection speed, we propose and demonstrate on an operational SEM a fast method to sparsely sample and reconstruct smooth images. To accurately localize the electron probe position at fast scan rates, we model the dynamics of the scan coils, and use the model to rapidly and accurately visit a randomly selected subset of pixel locations. Images are reconstructed from the undersampled data by compressed sensing inversion using image smoothness as a prior. We report image fidelity as a function of acquisition speed by comparing traditional raster to sparse imaging modes. Our approach is equally applicable to other domains of nanometer microscopy in which the time to position a probe is a limiting factor (e.g., atomic force microscopy), or in which excessive electron doses might otherwise alter the sample being observed (e.g., scanning transmission electron microscopy).

Keywords: scanning electron microscope, SEM, sparse reconstruction, compressed sensing

1 INTRODUCTION

Electron microscopes are used in neuroscience, microbiology and materials science for high-resolution imaging and subsequent structural or compositional analysis. In particular, many applications that utilize a scanning electron microscope (SEM) require imaging millimeters or even centimeters of material at nanometer resolutions, leading inevitably to semi-autonomous operation of a SEM, months of around-the-clock collection time [1, 2], and vast quantities of data.

Many recent efforts have addressed the problem of collecting large mosaics of a specimen [3–5]. Engineering advances (for example, [6]) have allowed greater throughput by allowing very wide field-of-view images to reduce image tile overlap and stage movement, and by providing high scan rates. Nevertheless, even these well-engineered systems are still physically constrained—due to the single-detector arrangement, the electron probe visits each pixel location in raster-scan order and dwells for a time proportional to the desired SNR. Thus, high-SNR, nm-resolution images taken over large mosaics can lead to prohibitively long data collection times.

In this paper, we propose and demonstrate on an operational SEM a sparse imaging method for smooth images, in which the electron probe measures only a subset of locations on the specimen. The approach is inspired by compressed sensing theory to guarantee that the smooth image can be recovered from undersampled data. Since the number of measurements is roughly

^{*} corresponding author: hander@sandia.gov

[†] Sandia National Laboratories is a multi-program laboratory managed and operated by Sandia Corporation, a wholly owned subsidiary of Lockheed Martin Corporation, for the U.S. Department of Energy's National Nuclear Security Administration under contract DE-AC04-94AL85000.

proportional to the data collection time, we can increase imaging throughput while maintaining image quality. Importantly, the imaging speedup provided by this approach is *in series* with speedups obtained via technological and engineering advances.

Our proposed method is applicable to other domains of nanometer microscopy in which speed is a limiting factor, such as atomic force microscopy (AFM). In [7], the authors apply compressed sensing for video-rate AFM and demonstrate results on a working instrument. Their goal for video-rate imaging is aided by a fixed, deterministic scan pattern that permits fast image reconstruction, but includes appreciable gaps that precludes universality [7]. Hu et al. recently addressed high-throughput image acquisition for neural circuitry by acquiring a few low resolution tomographic slices of tissue, then reconstructing a super-resolved 3D image by using 3D dictionary atoms learned from a high-resolution training set [8]. Recently, Binev et al. investigated the applicability of compressed sensing to scanning transmission electron microscopes (STEMs) to reduce electron dose rates that might otherwise structurally alter or destroy the sample being observed [9]. We note that the dose rate motivation is equally applicable to the SEM case, in which certain biological or dielectric materials may exhibit charging artifacts if the dose rate is too high. In [9], concepts are validated via numerical simulations of a STEM.

The chief contribution of this paper is a demonstration of sparse sampling and compressed sensing image recovery using an operational SEM. A fast recovery method is derived using the split Bregman formulation [10]. In order to implement our method on an operational tool, we account for nontrivial dynamics of the SEM scan coils through modeling and prediction.

In Section 2 we review pertinent elements of electron microscopy. In Section 3, we introduce a sparse sampling and exact recovery method, motivated by foundational work in compressed sensing, and show simulated reconstruction performance for smooth images. Hardware implementation and results from our experiments are discussed in Section 4. We conclude with a summary of our work in Section 5.

Throughout the paper boldface variable in capital letters such as \mathbf{F} , \mathbf{U} will denote matrices. The lowercase boldface variables, such as \mathbf{x} , or \mathbf{y} denote vectors, while non-boldface both lower-case and upper case, such as M and δ denote scalars.

2 BACKGROUND

SEMs are often a tool of choice for imaging biological, geological or material science specimens. Electron microscopes provide much higher magnifications than do optical microscopes. Fundamentally, the diffraction limit in electron microscopes is about 10^3 better than optical microscopes, down to sub-nanometer levels for typical electron energies. In addition, SEMs have a large depth of field, allowing a specimen to be in focus even when its topography exhibits high variability.

A SEM acquires images by raster scanning a focused beam of electrons across the sample, typically in raster-order. At each location, electrons in the incident beam interact with sample, producing various signals about the composition or topography of the sample’s surface. These signals may be detected and digitally assigned to the image pixel value at the corresponding sample location. The electron probe is then repositioned via electromagnetic or electrostatic deflection to the subsequent pixel location. Typically, the electron probe is much smaller than the distance between pixel locations.

Backscatter electron (BSE) emissions are high-energy electrons that originate in the electron beam and are reflected back out of the interaction volume on the sample via elastic scattering. Materials composed of heavy elements provide more opportunities for elastic scattering than do lighter elements, so that images created from BSE emissions provide sharp contrast at boundaries of different chemical composition. Secondary electrons (SE) are much lower-energy electrons that are dislodged from orbitals of specimen atoms through inelastic scattering with electrons in the incident beam. Due to their low energies, only SE emissions within the first

few nanometers of the sample surface radiate into the chamber. Thus SE images are primarily topographical.

Detectors have been designed to detect BSE and SE emissions separately. BSE detectors may be made from semiconductor materials and are positioned to leverage the higher energies of BSE emissions, which essentially travel in line-of-sight trajectories inside the chamber. In contrast, SE emissions are often detected by an Everhart-Thornley (E-T) detector, which attracts SEs to an electrically biased grid via a positive voltage bias which does not significantly deflect BSE emission trajectories. (However an E-T detector will respond to BSEs in its direct line of sight.) Secondary electrons attracted through the biased grid are further accelerated to a scintillator, which emits photons that are transported outside the SEM chamber. Using a photomultiplier tube, the photons are subsequently amplified to an intensity that can be readily captured. Sources of noise in the SE detection process include SE emissions originating from locations not illuminated by the electron probe (e.g., from backscatter electrons interacting with the chamber), line of sight BSEs, and detector noise introduced in one of the several stages of E-T detection. Noise for both BSE and SE images is multiplicative (Poisson-like), wherein the noise power is proportional to the signal intensity.

In order to produce high-quality SEM images, long (on the order of microseconds) integration times per pixel (alternatively, many digital samples per pixel) are required to reduce noise. In the best case with independent measurements, one could expect SNR improvement that grows like \sqrt{n} ; however, non-trivial detector response times and other factors necessitate longer integration times. In sum, well-engineered systems are SNR-limited in their data acquisition speed, and can require months to collect millimeters or centimeters of data for some applications.

One engineering challenge that often limits SEM speed is that the scanning coils, used to deflect the incident beam to the desired pixel location on the sample, have non-negligible dynamics. In most SEMs, the deflection is done with two or more sets of electromagnetic coils (at least one for each scan direction). A current is driven through these coils, which creates a magnetic field that deflects the moving electrons as they travel down the column. In addition to the inductance in the coils, stray capacitance and wire resistance creates a dynamic system which cannot respond instantaneously to changes in current. Additionally, the amplifiers used to drive the coils exhibit a non-negligible dynamic response. The combination of these systems creates a non-trivial dynamic system that can affect signals with frequency content as low as tens or hundreds of kHz. As a result, the actual location of the beam is often not the same as the commanded location, which creates image distortion unless some compensation is done. To mitigate these effects, SEMs are carefully calibrated at a variety of magnifications and speeds to compensate for coil dynamics and generally operate in a raster scan mode where the beam always moves at a constant speed in the same direction when an image is being taken, as opposed to a “meander” scan where the beam is driven back and forth which can create image artifacts that appear hysteretic. Beam dynamics are more problematic when a non-trivial beam motion is used to sample the data, such as when varying speeds or directions are used. The dynamical response of the electron probe scan coils is investigated further in Section 4.

3 SPARSE SAMPLING

The degrees of freedom of typical electron microscope images are many fewer than the number of image pixels. Foundational contributions in compressed sensing guarantee that an N -pixel image \mathbf{x} —which can be described by K coefficients in some compression basis Ψ —can be exactly recovered in only $M = O(K \log \frac{N}{K})$ linear measurements of the form $\mathbf{y} = \Phi \mathbf{x}$. The tightest guarantee to date holds when $\mathbf{A} = \Phi \Psi$ satisfies the restricted isometry property (see [11]), which guarantees recovery using basis pursuit:

$$\min_{\mathbf{x}} \quad \|\Psi^T \mathbf{x}\|_1 \quad \text{s.t.} \quad \Phi \mathbf{x} = \mathbf{y}.$$

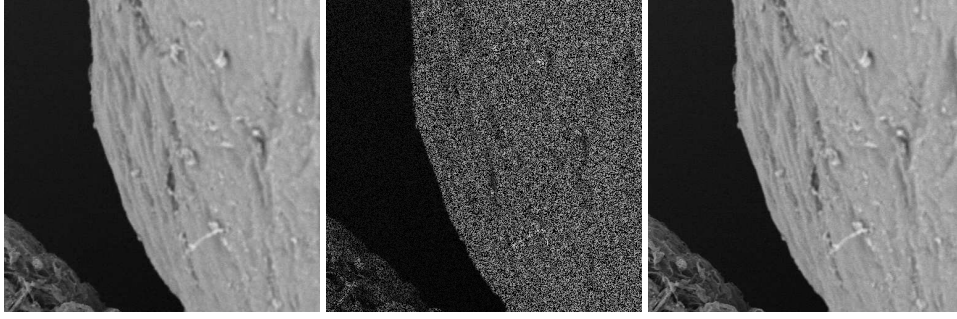


Fig. 1. (left) An excised 512×512 block from a SEM monograph of *Amorphophallus titanium* pollen; (center) simulated 50% random undersampling; (right) reconstruction using our method with block-DCT as a sparsifying basis (PSNR is 36 dB).

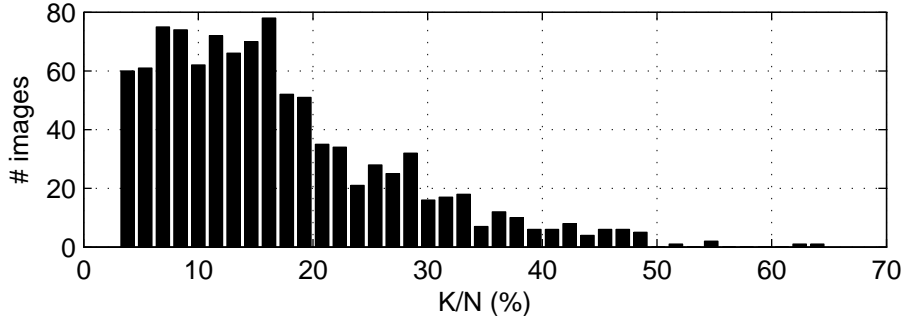


Fig. 2. The sparsity of Dartmouth public SEM images, where sparsity is measured by counting the number of block-DCT coefficients K that account for at least 99.75% of the image energy. The average sparsity is 17%, with half of all images less than 15% sparse, and three-quarters less than 20% sparse.

It should be noted that for arbitrary \mathbf{A} , certifying that the restricted isometry property holds is combinatoric in M . Although mutual coherence $\mu(\Phi, \Psi)$ provides a looser guarantee on reconstruction from $M = O(\mu K \log N)$ measurements, it is trivial to compute [12].

Electron microscope images are smooth and are often compressed via block-DCT or wavelet compression schemes using JPEG or JPEG-2000 standards, respectively, while still maintaining high image fidelity. To assess image sparsity of typical electron microscopy images, we gathered 1022 electron microscopy images (SEM, TEM and E-SEM) from the Dartmouth public domain gallery at <http://www.dartmouth.edu/~emlab/gallery>. The images are of a variety of different specimens in biology, geology and materials, and over a wide range of magnifications and image sizes. To standardize analysis, we excised the center 512×512 of each image to remove banners and rescaled images to $[0, 1]$ grayscale values. For each 512×512 image, we computed the sparsity K by counting the number of large coefficients in the block-DCT domain (32×32 blocks) that accounted for at least 99.75% of the total coefficient energy. A histogram of the results is shown in Figure 2.

3.1 Split Bregman Interpolation

In this section we outline a fast recovery/interpolation method for sparsely sampled images. Given sparsely sampled measurements $\mathbf{y} = \Phi \mathbf{x} + \mathbf{n}$, where Φ is a subset of rows of identity \mathbf{I}

and \mathbf{n} is noise with power σ^2 , we reconstruct the image by solving regularized basis pursuit:

$$\begin{aligned} \min_{\mathbf{x}} \quad & \|\Psi^T \mathbf{x}\|_1 + \|\nabla \mathbf{x}\|_1 \\ \text{s.t.} \quad & \|\mathbf{y} - \Phi \mathbf{x}\| \leq \sigma^2. \end{aligned} \quad (1)$$

Motivated by good JPEG compressibility of SEM images, and by the low mutual coherence between the DCT basis and image-domain sampling, we choose Ψ to be a block-DCT basis with 32×32 pixel blocks. The total variation regularizer $\|\nabla \mathbf{x}\|_1 = \sum_i \sqrt{|\nabla_h \mathbf{x}|_i|^2 + |\nabla_v \mathbf{x}|_i|^2}$ in (1) is included for denoising and to promote smooth boundaries between blocks.

Equation (1) can be solved efficiently using the split Bregman method [10], which recasts the constrained problem in (1) into an unconstrained problem of the form

$$\min_{\mathbf{x}} \|\Psi^T \mathbf{x}\|_1 + \|\nabla \mathbf{x}\|_1 + \frac{\mu}{2} \|\mathbf{y} - \Phi \mathbf{x}\|.$$

We follow the compressed sensing MRI derivation in [10], noting that our problem structure differs since we collect image-domain samples rather than Fourier-domain samples. Letting $\mathbf{w} = \Psi^T \mathbf{x}$, $\mathbf{u} = \nabla_u \mathbf{x}$ (horizontal gradient), $\mathbf{v} = \nabla_v \mathbf{x}$ (vertical gradient) and shorthand $\|(\mathbf{u}, \mathbf{v})\|_2 = \sum_i \sqrt{|\mathbf{u}_i|^2 + |\mathbf{v}_i|^2}$, apply the split Bregman formulation so that the problem can be solved iteratively to arbitrary precision. In particular, at the k th iteration, solve

$$\begin{aligned} \min_{\mathbf{x}, \mathbf{u}, \mathbf{v}, \mathbf{w}} \quad & \|\mathbf{w}\|_1 + \|(\mathbf{u}, \mathbf{v})\|_2 + \frac{\mu}{2} \|\Phi \mathbf{x} - \mathbf{y}\|_2^2 \\ & + \frac{\lambda}{2} \|\mathbf{u} - \nabla_u \mathbf{x} - \mathbf{b}_u^k\|_2^2 + \frac{\lambda}{2} \|\mathbf{v} - \nabla_v \mathbf{x} - \mathbf{b}_v^k\|_2^2 + \frac{\gamma}{2} \|\mathbf{w} - \Psi^T \mathbf{x} - \mathbf{b}_w^k\|_2^2, \end{aligned} \quad (2)$$

and then update the so-called Bregman parameters \mathbf{b}_u^k , \mathbf{b}_v^k and \mathbf{b}_w^k via

$$\mathbf{b}_u^{k+1} = \mathbf{b}_u^k + (\nabla_u \mathbf{x}^{k+1} - \mathbf{u}^{k+1}) \quad (3)$$

$$\mathbf{b}_v^{k+1} = \mathbf{b}_v^k + (\nabla_v \mathbf{x}^{k+1} - \mathbf{v}^{k+1}) \quad (4)$$

$$\mathbf{b}_w^{k+1} = \mathbf{b}_w^k + (\Psi^T \mathbf{x}^{k+1} - \mathbf{w}^{k+1}). \quad (5)$$

The merit in the “split” Bregman formulation is that the ℓ_1 and ℓ_2 portions of (2) have been decoupled, allowing a simple solution via alternating minimizations. The variables involving ℓ_1 norms are solved efficiently via element-wise shrinkage:

$$\mathbf{u}_i^{k+1} = \frac{\max(\mathbf{s}_i^k - \frac{1}{\lambda}, 0)}{\mathbf{s}_i^k} ((\nabla_u \mathbf{x}^k)_i + \mathbf{b}_{u,i}^k) \quad (6)$$

$$\mathbf{v}_i^{k+1} = \frac{\max(\mathbf{s}_i^k - \frac{1}{\lambda}, 0)}{\mathbf{s}_i^k} ((\nabla_v \mathbf{x}^k)_i + \mathbf{b}_{v,i}^k) \quad (7)$$

$$\mathbf{w}_i^{k+1} = \text{shrink} \left((\Psi^T \mathbf{x}^{k+1})_i + \mathbf{b}_{w,i}^k, \frac{1}{\gamma} \right) \quad (8)$$

where

$$\mathbf{s}_i^k = \sqrt{|(\nabla_u \mathbf{x}^k)_i + \mathbf{u}_i^k|^2 + |(\nabla_v \mathbf{x}^k)_i + \mathbf{v}_i^k|^2}$$

and

$$\text{shrink}(x, \rho) = \text{sgn}(x) \max(|x| - \rho, 0).$$

Solving (2) for \mathbf{x} yields

$$\begin{aligned} (\mu \Phi^T \Phi - \lambda \Delta + \gamma \mathbf{I}) \mathbf{x}^{k+1} = \\ \mu \Phi^T \mathbf{y} + \lambda \nabla_u^T (\mathbf{u}^k - \mathbf{b}_u) + \lambda \nabla_v^T (\mathbf{v}^k - \mathbf{b}_v) + \gamma \Psi (\mathbf{w}^k - \mathbf{b}_w), \end{aligned} \quad (9)$$

where we have assumed that $\Psi^T \Psi = \mathbf{I}$, and used $\Delta = -\nabla^T \nabla$ to represent the discrete Laplacian operator. Note that unlike the MRI example introduced in [10], the system in (9) is not circulant since $\Phi^T \Phi$ is non-constant along its main diagonal. Therefore, the system cannot be diagonalized by the discrete Fourier transform to arrive at an exact solution. Nevertheless, as noted in [10], an approximate solution to \mathbf{x}^k at each iteration suffices, since extra precision is wasted in the Bregman parameter update step. A few steps of the conjugate gradient method may suffice for arbitrary Φ , but for the special case in which Φ is a subset of the rows of identity, we utilized a more efficient approach. Indeed, we have found that our algorithm converges when approximating $\Phi^T \Phi$ as the nearest circulant matrix \mathbf{C} , where nearness is measured in terms of the Frobenius norm $\|\Phi^T \Phi - \mathbf{C}\|_F$. This results in $\Phi^T \Phi \approx \mathbf{C} = a\mathbf{I}$, where a is the average of the elements along the main diagonal of $\Phi^T \Phi$. The approximation error is bounded by $\|\Phi^T \Phi - a\mathbf{I}\|_F = \sqrt{N}/2$ at $M = N/2$. Employing the circulant approximation allows (9) to be solved efficiently using Fourier diagonalization.

In summary, our application of the split Bregman formulation for basis pursuit interpolation consists of an inner loop that solves (2) via (6)–(8) and a circulant approximation to (9), and an outer loop that updates the Bregman parameters via (3)–(5). For typical images on the interval $[0, 1]$, we found that $\mu = \lambda = 1$ and $\gamma = 10^{-2}$ are reasonable values for reconstruction. In our implementation, we use two iterations of the inner loop, and 150 iterations of the outer loop for noiseless data, though 20–50 iterations are typically sufficient to produce high-quality reconstructions. An example reconstruction from $M = N/2$ randomly selected samples is shown in Figure 1.

3.2 Simulations and Results

Using the proposed recovery method in Equation (1), we simulated reconstruction of the public domain Dartmouth images from sparse samples. For each 512×512 excised and standardized image \mathbf{x} , we simulated sparse sampling by choosing M pixels at random from the image, where M/N is swept from 10% to 100%. Then, we reconstructed the image using the approach described in Section 3.1. The reconstructed image $\hat{\mathbf{x}}$ is deemed a “success” if $\|\mathbf{x} - \hat{\mathbf{x}}\|_2^2 / \|\mathbf{x}\|_2^2 \leq 0.25\%$, that is, if the reconstruction accounts for at least 99.75% of the image energy. Reconstruction results are shown in Figure 3.

We wondered whether simple linear interpolation could be used for successful recovery, since it is both simple and very efficient. (For the reconstruction in Figure 1, our method took 18 seconds for 50 iterations using non-optimized MATLAB code with a 2.66 GHz Intel Xeon processor, whereas a similar reconstruction using MATLAB’s `griddata` for linear interpolation took only 2 seconds.) Indeed, for noiseless measurements, linear interpolation performs nearly as well as our proposed method, with only $\approx 5\%$ less area of the curve in Figure 3. However, linear interpolation is brittle, performing significantly worse in the presence of only a small amount of noise. Figure 3 shows $\approx 50\%$ less area under the curve than our method using the same noisy measurements. (Noise was multiplicative: for pixel intensity η , we added zero-mean white Gaussian noise with variance $\eta/100$). Thus, linear interpolation may be attractive as a “quick-look” option, but the proposed method is preferred for high-quality reconstruction.

4 EXPERIMENTS

In this section, we demonstrate on an operational SEM our sparse sampling and recovery method for fast electron microscopy. The experiments were conducted using a commercially available SEM column with custom electronics to drive the beam location and sample the detector. A Zeiss GmbH (Oberkochen, Germany) column was used with a Schottky thermal field emission source and GeminiTM optics. A nominal beam energy of 10 keV was used with a 10 μm aperture, resulting in a beam current of approximately 200 pA.

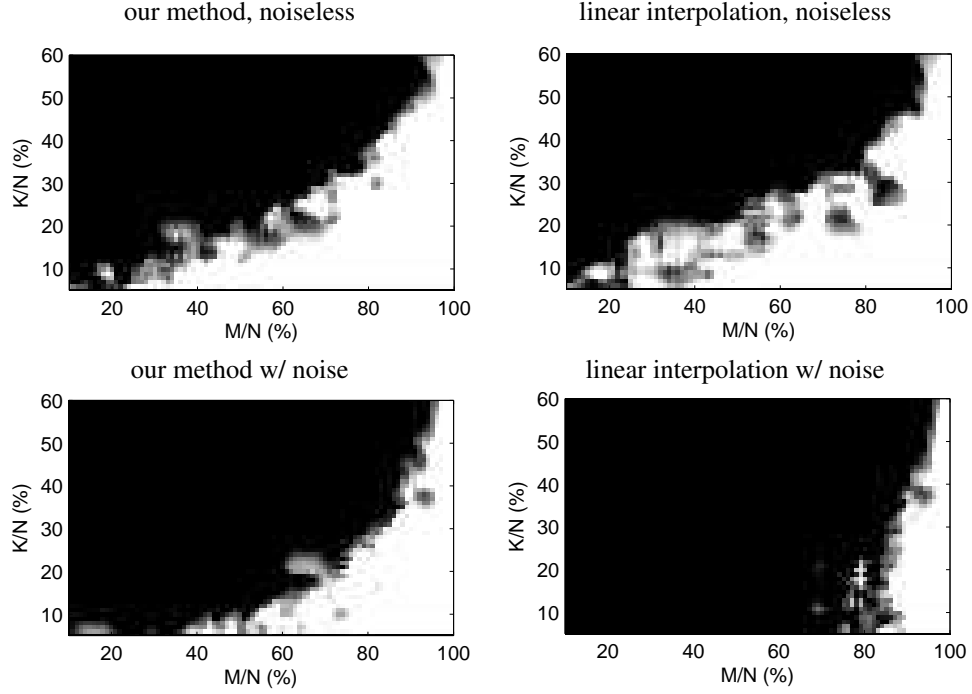


Fig. 3. Reconstruction phase transitions using the Dartmouth images whose sparsity histogram is shown in Figure 2. The shading indicates how frequently an image with a given sparsity K/N was “successfully” reconstructed (accounted for at least 99.75% of the image energy) at a given undersampling rate M/N ; the shading ranges from 0% (black) to 100% (white). For noiseless measurements (top row), linear interpolation (right) is only slightly worse than our method (left) in terms of area under the curve, but is significantly worse when a small amount of measurement noise is included (bottom row).

The incident beam was deflected onto the sample using the standard scanning coils and current amplifiers in the column. However, custom electronics were used to set the desired beam location using an external scan mode. The magnification (and consequently the field of view) was set using the standard column controls. Once this was determined, pixels in the field of view can be visited by driving a voltage of -10 V to +10 V, which is converted to a current in the coil amplifiers. For example, in the horizontal direction, driving -10 V would place the beam at the far left of the field of view and +10 V would place the beam at the far right. The same is true in the vertical direction. A digital to analog converter (DAC) was used to drive the desired voltages. The detector was sampled using an analog to digital converter (A/D) that was synchronized to the DAC. The A/D and DAC were implemented using a National Instruments (Austin, TX) PCI-6110 multi-function data acquisition system. This system has a maximum frequency of 2.5 MHz with two analog outputs, an output resolution of 16 bits per sample and an input resolution of 12 bits per sample.

We achieve variable dwell time by digitally averaging multiple samples at the same pixel location. A basic dwell time of 400 ns using one sample per pixel results in low-SNR images, while a high-SNR dwell time of 6.4 μ s achieved by averaging 16 samples per pixel. A high-SNR image of the surface of a Gibeon meteorite collected in the manner just described is shown in Figure 4, along with *simulated* sparse sampling and subsequent image recovery.

It should be noted that on an operational SEM, nontrivial dynamics of the electron probe scanning system create a mismatch between the desired and actual measurement locations on

the sample. The effect is less pronounced in typical raster-scan mode in which the electron probe follows the same trajectory during each scan line, leading only to a nonlinear stretch of the image. However, in our sparse imaging embodiment, the interval between randomly-selected pixel locations within a scan line is highly variable, so that the effect of the dynamics is pronounced, and the measured location differs from the desired location. Therefore, we investigate scan coil dynamics and mitigation in the following subsections.

4.1 Scan coil dynamics

In order to characterize the dynamics of the amplifiers and scan coils, we commanded a step-wise jump in position from one extreme of the beam's scanning range to the other over a calibration sample. While the electron beam was in transit, we recorded the output of the secondary electron detector. This step-scanning method produced a smeared scan of the sample. Comparing this with a very slow raster scan of the same sample allowed us to plot the transit as a function of time. (See Figure 6.)

We found the dynamics of the beam to be slow compared to the sampling period (400 ns). The 90% rise time was approximately $12 \mu\text{s}$, the 99% rise time about $32 \mu\text{s}$, and the 99.9% rise time approximately $1/4 \text{ ms}$, or more than 600 samples. Note that the 99.9% rise time is relevant; when making scans of several thousand pixels per line, an error of 0.1% corresponds to several pixels.

The lowest order linear model to fit the data points well was fifth-order of the form

$$\frac{d^5 x(t)}{dt^5} = a_0(\hat{x}(t) - x(t)) - a_1 \frac{dx(t)}{dt} - a_2 \frac{d^2 x(t)}{dt^2} - a_3 \frac{d^3 x(t)}{dt^3} - a_4 \frac{d^4 x(t)}{dt^4}, \quad (10)$$

where $x(t)$ is the true one-dimensional probe position (in pixels) at time t , $\hat{x}(t)$ is the desired position, and the best-fit parameters $\{a_0, \dots, a_4\}$ are listed in Table 1. The same dynamical model was used for both horizontal and vertical beam deflection.

parameter	value
a_0	4.42×10^{-4}
a_1	8.20×10^{-3}
a_2	5.49×10^{-2}
a_3	2.46×10^{-1}
a_4	4.60×10^{-1}

Table 1. Parameters for the best fit fifth-order model of scan coil dynamics in Equation (10).

4.2 Sparse Sampling Demonstration

We demonstrated the proposed sparse sampling method in an operational SEM. Mirroring Figure 4, we commanded the electron probe to visit 10%, 30% and 50% of the sample locations (chosen at random) in vertical-raster order, and to dwell for $6.4 \mu\text{s}$ (16 samples per pixel) at each location. We used a 4/5 Runge-Kutta method to solve Equation (10) in order to predict the actual location of the electron probe. The result is that the 16 samples per pixel are actually distributed across multiple pixel locations as the electron probe is in transit, as shown in Figure 5.

We image a portion of the Gibeon meteorite sample at $800\times$ magnification at a working distance of 4.7 mm. Due to the close working distance, we collected samples with an in-lens SE detector. Brightness and contrast for each sparse sampling collection is fixed at 76% and 41%, collectively.

Results for the sparse sampling collection and reconstruction are shown in Figure 5. For $M/N = 10\%$, the reconstruction exhibits some smearing along the vertical path of the electron

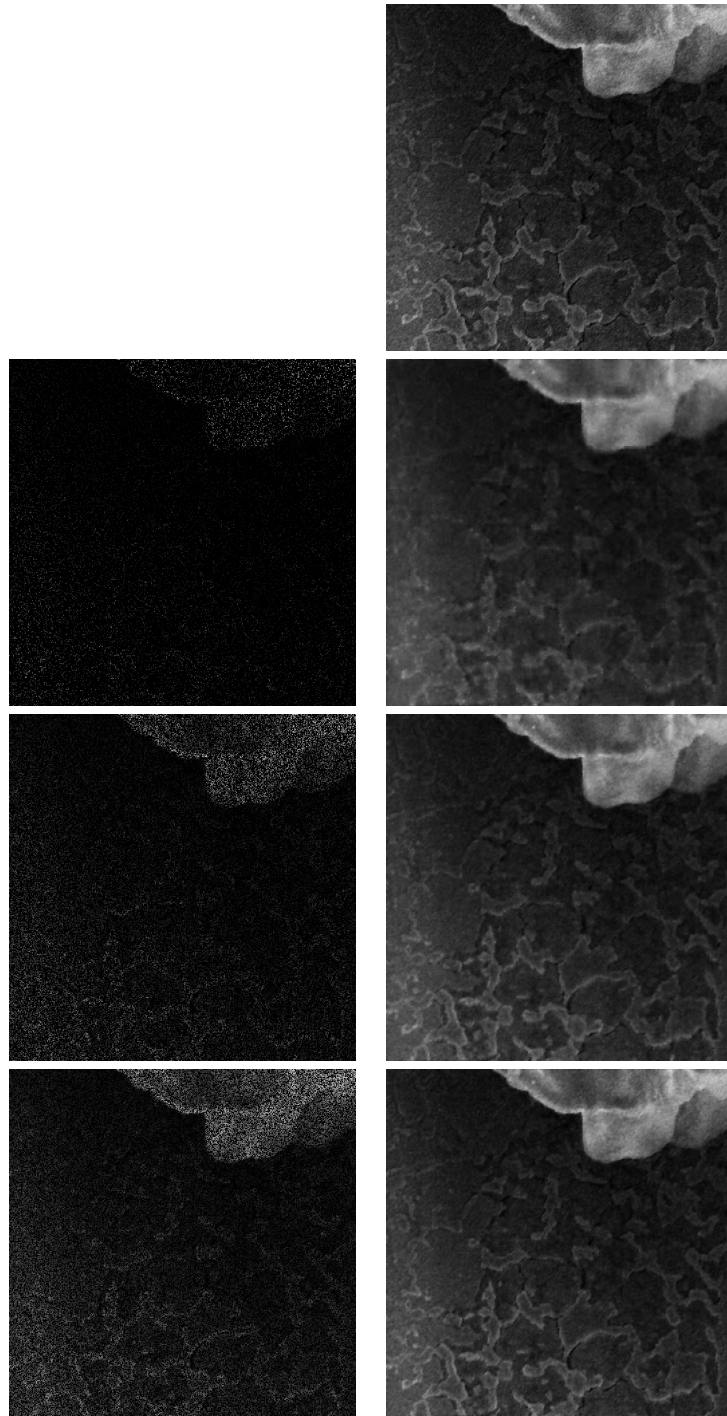


Fig. 4. (top) Original section of a high-SNR micrograph from our SEM of a particle atop the surface Gibeon meteorite slice; (2nd row) simulated 10% sparse samples (left) and reconstruction (right); (3rd row) simulated 30% sparse samples (left) and reconstruction (right); (4th row) simulated 50% sparse samples (left) and reconstruction (right)

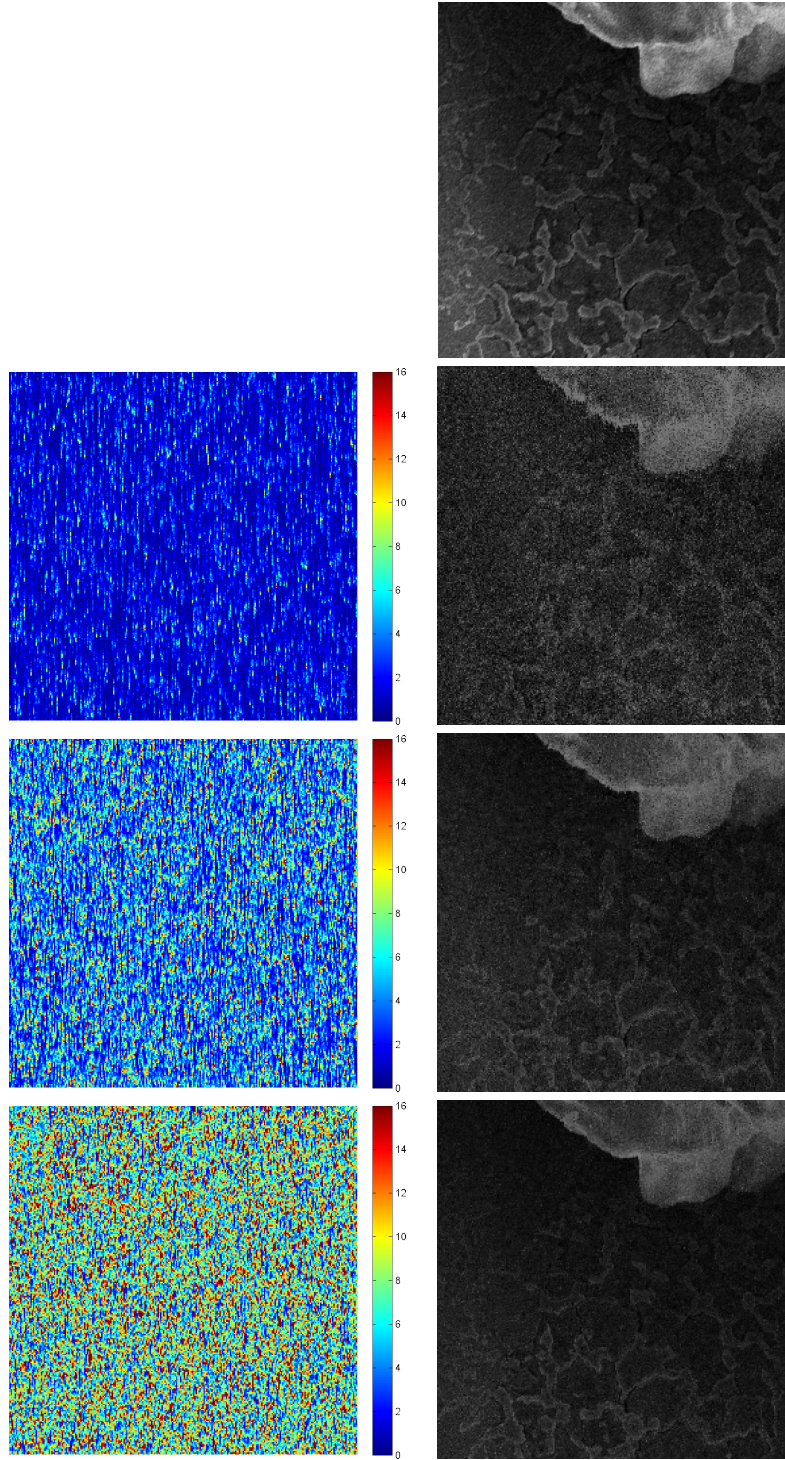


Fig. 5. (top) Standard SEM image of the Gibeon sample; (2nd row) 10% sparse, modeled sample locations (left) and reconstruction (right); (3rd row) 30% sparse, modeled sample locations (left) and reconstruction (right); (4th row) 50% sparse, modeled sample locations (left) and reconstruction (right). The colors in the left column represent the number of times the probe visited the given pixel. The electron probe scans in the vertical direction. In addition to sample quality, notice the difference in sample charging.

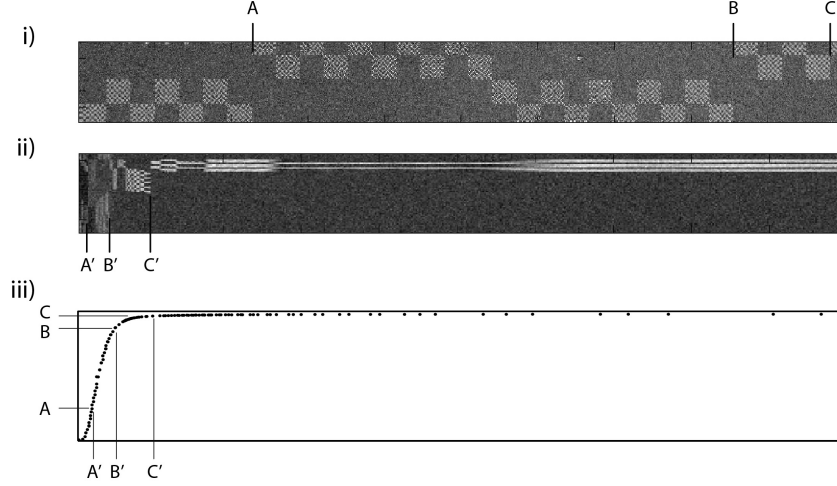


Fig. 6. Measurement of the scan coil's dynamic response. **i)** A slow scan was performed to obtain a nearly dynamics-free image of the sample. **ii)** The beam was stepped from one extreme of the scan range to the other while recording from the secondary electron detector. Landmarks on both images were located. **iii)** The positions of the landmarks were plotted relative to each other to obtain data points along the step response curve.

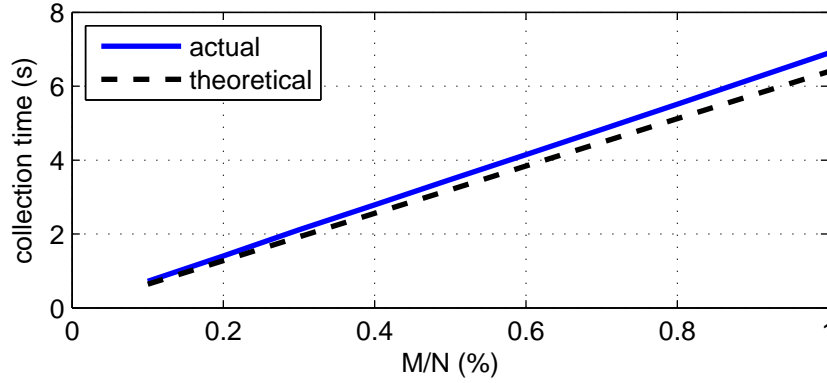


Fig. 7. Actual and predicted collection time as a function of undersampling rate M/N .

probe, which can be attributed to large electron probe velocities and small errors in the 5th order model. Acceptable image reconstruction is achieved for $M/N \geq 30\%$, corresponding to over $3\times$ increase in data throughput. Notice also that the for smaller M/N , the lower average electron dose rates contribute to less charging on the sample (manifest by the slight glow on the left-hand-side of the image).

The measured image acquisition time for collecting every pixel of a 1000×1000 image with 16 samples per pixel is 6.9s (expected 6.4s at 2.5 MHz). Using sparse sampling factors of 10%, 30% and 50%, we measured image collection times 0.7s ($9.9\times$ speedup), 2.1s ($3.3\times$ speedup), and 3.5s ($2.0\times$ speedup), respectively, for 1000×1000 images. These collection times are only slightly more than what would be predicted at 2.5 MHz, which can be ascribed to software overhead. Nevertheless, the collection time indeed grows linearly with the number of samples M , as shown in Figure 7.

5 CONCLUSIONS

We have demonstrated sparse sampling in an operational SEM, with acceptable image quality achieved at $3\times$ speedup for the sample we tested. This was accomplished by commanding the electron probe to visit a randomly-selected subset of pixel locations, predicting the actual locations via a 5th-order dynamical model, then recovering the image using a split-Bregman formulation of regularized basis pursuit that leveraged block-DCT as a sparsifying basis.

Like most systems based on compressed sensing, our sparse imaging method achieves efficient data collection at the expense of greater off-line computation. Although fairly efficient, our method still requires an order of magnitude more time to reconstruct the image than was required to collect the data. This is acceptable since, in contrast to data collection, image recovery may be easily distributed across many CPUs. Evaluating the quality of other approaches for image recovery based on dictionary learning or image inpainting is a topic for future research.

ACKNOWLEDGEMENTS

The authors thank Kelvin Lee for aggregating and analyzing the Dartmouth microscopy images.

References

- [1] K. L. Briggman and W. Denk, "Towards neural circuit reconstruction with volume electron microscopy techniques," *Current Opinion in Neurobiology* **16**, 562–570 (2006).
- [2] J. R. Anderson, B. W. Jones, C. B. Watt, M. V. Shaw, J.-H. Yang, D. DeMill, J. S. Lauritzen, Y. Lin, K. D. Rapp, D. Mastronarde, P. Koshevoy, B. Grimm, T. Tasdizen, R. Whitaker, and R. E. Marc, "Exploring the retinal connectome," *Molecular Vision* **17**, 355–379 (2011).
- [3] K. Ogura, M. Yamada, O. Hirahara, M. Mita, N. Erdman, and C. Nielsen, "Gigantic montages with fully automated FE-SEM," *Microsc. Microanal.* **16** (Suppl 2), 52–63 (2010).
- [4] A. R. Shiveley, P. A. Shade, A. L. Pilchak, J. S. Tiley, and R. Kerns, "A novel method for acquiring large-scale automated scanning electron microscope data," *Journal of Microscopy* **244**, 181–186 (2011).
- [5] K. J. Hayworth, N. Kasthuri, R. Schalek, and J. W. Lichtman, "Automating the collection of ultrathin serial sections for large volume TEM reconstructions," *Microsc. Microanal.* **12** (Suppl 2), 86–87 (2006).
- [6] M. Wiederspahn, "Analytical power for the sub-nanometer world," *Imaging & Microscopy* **11**, 25–26 (2009).
- [7] B. Song, N. Xi, R. Yang, K. W. C. Lai, and C. Qu, "Video rate atomic force microscopy (AFM) imaging using compressive sensing," *Proc. IEEE Conf. Nanotechnology*, 1056–1056 (2011).
- [8] T. Hu, J. Nunez-Iglesias, S. Vitaladevuni, L. Scheffer, S. Xu, M. Bolorizadeh, H. Hess, R. Fetter, and D. Chklovskii, "Super-resolution using sparse representations over learned dictionaries: Reconstruction of brain structure using electron microscopy," *arXiv preprint arXiv:1210.0564* (2012).
- [9] P. Binev, W. Dahmen, R. DeVore, P. Lamby, D. Savu, and R. Sharpley, *Modeling Nanoscale Imaging in Electron Microscopy*, ch. Compressed Sensing and Electron Microscopy, 73–126. Springer (2012).
- [10] T. Goldstein and S. Osher, "The split Bregman method for L1-regularized problems," *SIAM Journal on Imaging Sciences* **2**(2), 323–343 (2009).
- [11] E. Candès, "The restricted isometry property and its implications for compressed sensing," *Comptes rendus-Math.* **346**(9–10), 589–592 (2008).
- [12] D. Donoho, M. Elad, and V. Temlyakov, "Stable recovery of sparse overcomplete representations in the presence of noise," *Information Theory, IEEE Transactions on* **52**(1), 6–18 (2006).